Adaptive Finite Volume Upwind Approach on Mixed Quadrilateral-Triangular Meshes

C. J. Hwang* and S. J. Wu†

National Cheng Kung University, Tainan, Taiwan 70101, Republic of China

An adaptive cell-vertex finite volume upwind approach on unstructured mixed quadrilateral-triangular meshes, where the quadrilaterals are directionally stretched in the flow regions having one-dimensional features, has been developed to solve the unsteady Euler equations. In the present approach, the Runge-Kutta time integration, Roe's Riemann solver, MUSCL differencing with characteristic interpolation variables, a new treatment of the rotated extrapolation boundary condition, and a modified technique of the global/local regeneration for directionally stretched meshes are included. By using different combinations of interpolation variables, limiter functions, and numerical implementations of boundary conditions, a systematic study is made to understand the characteristics of the current approach. In this work, the isolated oblique shock problem, shock reflection at a wall, supersonic flow passing through a channel with a 4% circular arc bump, transonic flows around single- and two-element airfoils, as well as the shock propagation in a channel are investigated. It is concluded that the present solution procedure demonstrates good convergence performance and provides accurate and high-resolution results for the steady and unsteady inviscid flows.

Introduction

IN recent years, significant attention has been given to the development of numerical methods for solving the Euler equations on unstructured meshes. Several impressive central-difference-type schemes[1,2] and upwind approaches[3-5] were presented. Based on Roe's flux difference splitting,[6] Barth and Jespersen[3] utilized multidimensional monotone linear reconstruction procedures to create cell-centered and mesh-vertex schemes on triangular and quadrilateral control volumes. When a high-order reconstruction approach was used, Barth and Frederickson[4] developed a class of high-order-accurate schemes. By introducing so-called ghost nodes and employing MUSCL differencing with conserved variables, Whitaker et al.[5] presented a numerical procedure of a cell-vertex scheme on pure triangles. It is known that these approaches[3-5] place the upwind direction normal to the face of the computational cell across which the fluxes are computed and are thus mesh dependent.[7] To match the finite difference stencil to flow physics, rotated upwind algorithms were developed on structured rectangular grids.[7,8] Even though the rotated scheme can improve the resolution of the numerical solution, Dadone and Grossman[7] mentioned that their formulation requires the solution of two Riemann problems at each cell face. To maintain the simplicity of the mesh-dependent upwind solver while increasing its accuracy and robustness, an adaptive cell-vertex upwind scheme is developed in the present work. The numerical formulation presented by Whitaker et al.[5] is modified and extended to mixed quadrilateral-triangular meshes. For the current approach, the characteristic interpolation variables are employed in the MUSCL differencing. The mixed grid system, where directionally stretched quadrilaterals are created in the flow regions having one-dimensional features, is generated by improving the existing global/local mesh regeneration algorithm.[9]

One of the major difficulties in implementing cell-vertex schemes is the treatment of wall boundary conditions for

inviscid flow. On the triangular meshes, first- and second-order-accurate normal extrapolations, as well as the solution of conservation equations at the wall surface, have already been introduced in Ref. 5. For the normal extrapolations, flow tangency was enforced, and all flow variables were found from those of the interior nodes. When the Euler equations were solved at the wall boundary, a simple center difference method was used, and a normal extrapolation of entropy was performed to remove the spurious entropy generated by this approach. As mentioned in Ref. 5, a convergent solution of the blunt body flow could not be obtained by solving the governing equations at the wall. For the shock reflection problem, Dadone and Grossman[7] indicated that normal extrapolation can result in a possible inconsistency since even with infinitely small cell size an oblique shock may lie between the boundary surface and the nearest cell center. The characteristic boundary condition was employed and proved to give better results than normal extrapolation for this computational problem. More recently, Dadone[10] further inspected the characteristic boundary condition and revealed that some oscillations exist in the direction normal to the wall surface. Moreover, both simple extrapolation and characteristic treatment fail to give satisfactory results. Following this discussion, a new treatment of the boundary condition, which is based on the concept of rotated extrapolation, is developed in the present work. To evidence the capability of the current boundary treatment, the numerical results are compared to those obtained by using the normal extrapolation and the characteristic boundary condition.

In this paper, an adaptive cell-vertex finite volume upwind approach, which includes Roe's Riemann solver, MUSCL differencing with characteristic interpolation variables, a new rotated boundary treatment, and a modified global/local regeneration technique, is developed on mixed quadrilateral-triangular meshes. By incorporating Runge-Kutta time integration with the adaptive upwind space discretization, which was mentioned earlier, the isolated oblique shock problem, shock reflection at a wall, supersonic flow passing through a channel with a 4% circular arc bump, transonic flows over the single and two-element NACA-0012 airfoils, and shock propagation in a channel are investigated. Based on those numerical experiments, the present solution procedure is accurate, reliable and suitable for studying the steady and unsteady inviscid flows.

Governing Equations

By choosing the characteristic length and flow properties at the inlet or under freestream conditions as reference variables, the two-dimensional Euler equations can be written in nondimensional form for the Cartesian coordinate system:

$$\frac{\partial U}{\partial t} + \frac{\partial E}{\partial x} + \frac{\partial G}{\partial y} = 0 \tag{1}$$

where

$$U = \begin{bmatrix} \rho \\ \rho u \\ \rho v \\ e \end{bmatrix}, \quad E = \begin{bmatrix} \rho u \\ \rho u^2 + P \\ \rho u v \\ (e + P)u \end{bmatrix}, \quad G = \begin{bmatrix} \rho v \\ \rho u v \\ \rho v^2 + P \\ (e + P)v \end{bmatrix} \tag{2}$$

The unknown variables ρ, u, v, and e represent the gas density, velocity components in the x and y directions, and total energy per unit volume, respectively. The working fluid (air) is assumed to be perfect, and the pressure P is defined by

$$P = (\gamma - 1)\left[e - \frac{\rho}{2}(u^2 + v^2) \right] \tag{3}$$

where the ratio of specific heats γ is typically taken as being 1.4.

Numerical Algorithm

By integrating Eq. (1) over space and applying the Gauss theorem, the following integral form is obtained

$$\frac{\partial}{\partial t} \iint_{\Omega} U \, dA + \int_{\partial \Omega} (Ei + Gj) \cdot n \, dl = 0 \tag{4}$$

where n is the outward unit normal vector. The variable Ω is the domain of computation, and $\partial \Omega$ is the boundary of the domain. For the present cell-vertex scheme, the two-dimensional domain Ω is discretized into triangles and quadrilaterals, and the flow variables are stored at the vertices, such as V_i and V_j (see Fig. 1). By connecting the centroid of each polygon (triangle or quadrilateral) to the midpoints of its sides, the polygon is broken into subelements and a dual mesh is formed. As shown in Fig. 1, a dual mesh cell C_i is defined by the collection of subelements sharing the same vertex V_i, and the boundary of the cell is denoted by ∂C_i. Assuming that the flow variables at the vertex V_i have average values of the integrated variables in C_i, Eq. (4) can be written as:

$$\text{AREA}(C_i) \frac{\partial U}{\partial t} = -\int_{\partial C_i} F(n) \, dl \tag{5}$$

where $\text{AREA}(C_i)$ is the area of the cell C_i, and $F(n)$ is the flux oriented along the outward unit normal n [i.e., $F(n) = (n_x E + n_y G)$]. To achieve the time integration on the left-hand side of Eq. (5), a two-step Runge-Kutta method,[11] which re-

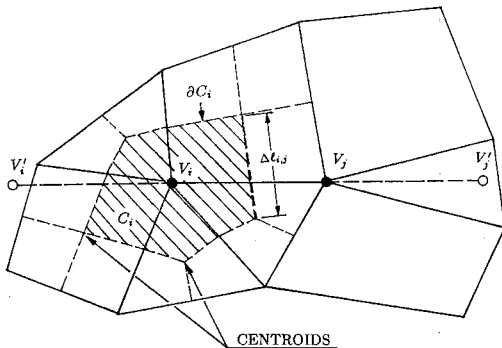sults in second-order time-accurate solutions, is employed for unsteady flows. A four-stage Runge-Kutta scheme with nonstandard weighting of the Runge-Kutta stages, local time steps, and residual smoothing[5] is introduced to study the steady flow problems. In the current cell-vertex formulation, the right-hand side of Eq. (5) is evaluated by

$$\int_{\partial C_i} F(n) \, dl = \sum_{j = L(V_i)} F_{i,j} \, \Delta l_{i,j} \tag{6}$$

where $L(V_i)$ is the list of vertices surrounding V_i, and the subscript j denotes the vertices contained in $L(V_i)$. $F_{i,j}$ represents the numerical approximation for the oriented flux across the dual cell edge having the boundary length $\Delta l_{i,j}$ (see Fig. 1). In this work, the terms n and $\Delta l_{i,j}$ of Eq. (6) are obtained by the area-averaged approach.[5]

To implement the upwind approach, Roe's flux difference splitting[6] is employed. The flux at the cell interface $F_{i,j}$ can be expressed as a function of two fluid dynamic states (U^L and U^R):

$$F_{i,j} = H(U^L, U^R) = \frac{1}{2}[F_L + F_R - |A|(U^R - U^L)] \tag{7}$$

where $|A|$ is a positive definite matrix formed from the flux Jacobian $\partial F / \partial U$,[6] and the superscripts R and L indicate the right and left fluid states, respectively. By equating both states to the properties stored at vertices V_i and V_j, first-order approximations for U and U_R can be obtained. To achieve a high-order upwind scheme, the left and right Riemann states U^L and U^R are found by a preprocessing approach. In this work, MUSCL differencing[12] is utilized to interpolate the properties at the cell interface using the variables stored at the cell vertices. In the interpolation procedure, both central and upstream differences are required. The ghost nodes V_i' and V_j' (see Fig. 1), which are located equidistantly along the line connecting V_i and V_j, are introduced. In order to evaluate state variables at ghost nodes, the simple interpolation technique,[5] originally formulated on pure triangles, is extended to the mixed quadrilateral-triangular meshes. In this work, the interpolation variables (conserved, primitive, or characteristic ones[7]) are combined with different limiter functions to understand the features of the current approach.

To prevent numerical oscillations near the high gradient regions, three limiters, which include the minimum-modulus (MINMOD)[12] and those presented by van Albada et al.[13] and Hemker and Koren,[14] are employed. In the following discussion, the variables at nodes V_i, V_j, V_i', and V_j' are denoted as Q_i, Q_j, Q_i', and Q_j', respectively. When the MINMOD limiter function is used, the MUSCL differencing formulas can be written as:

$$Q^L = Q_i + \frac{1}{4}\{(1 - \kappa)\overline{\Delta}_- + (1 + \kappa)\overline{\Delta}_+\}Q_i \tag{8}$$

$$Q^R = Q_j - \frac{1}{4}\{(1 - \kappa)\overline{\Delta}_+ + (1 + \kappa)\overline{\Delta}_-\}Q_j \tag{9}$$

$$\overline{\Delta}_- Q = \text{minmod}(\Delta_- Q, \beta \Delta_+ Q) \tag{10}$$

$$\overline{\Delta}_+ Q = \text{minmod}(\Delta_+ Q, \beta \Delta_- Q) \tag{11}$$

where the backward and forward differences are, respectively, $\Delta_-(Q_i) = Q_i - Q_i'$, $\Delta_+(Q_i) = Q_j - Q_i$, $\Delta_-(Q_j) = Q_j - Q_i$, and $\Delta_+(Q_j) = Q_j' - Q_j$. The parameter κ, which controls the spatial accuracy, is taken as being $\frac{1}{3}$, and the compression factor β is no greater than $(3 - \kappa)/(1 - \kappa)$. In Eqs. (10) and (11), the MINMOD function is defined as

$$\text{minmod}(a, b) = \text{sgn}(a) \max\{0, \min[a \, \text{sgn}(b), b \, \text{sgn}(a)]\} \tag{12}$$

In contrast to the discontinuous behavior of the MINMOD function, van Albada et al.'s limiter acts in a continuously

Fig. 1 Representative unstructured grid, dual cell, edge of an unstructured mesh, and locations of ghost nodes.

differentiable manner. By using van Albada et al.'s limiter, the MUSCL differencing formulas are expressed as follows:

$$Q^L = Q_i + \frac{s_1}{4} \{(1 - \kappa s_1)\Delta_- + (1 + \kappa s_1)\Delta_+\} Q_i \qquad (13)$$

$$Q^R = Q_j - \frac{s_2}{4} \{(1 - \kappa s_2)\Delta_+ + (1 + \kappa s_2)\Delta_-\} Q_j \qquad (14)$$

where

$$s_1 = s_2 = \frac{2\Delta_-\Delta_+ + \delta}{(\Delta_-)^2 + (\Delta_+)^2 + \delta} \qquad (15)$$

and δ is equal to 10^{-6}. For the limiter of Hemker and Koren, the MUSCL differencing formulas in Eqs. (13) and (14) are used with $s_1 = (3\Delta_+\Delta_-)/[2(\Delta_+)^2 + 2(\Delta_-)^2 - \Delta_-]$ and $s_2 = (3\Delta_+\Delta_-)/[2(\Delta_+)^2 + 2(\Delta_-)^2 - \Delta_+]$.

Rotated Boundary Conditions

In the present calculations, since the flows are inviscid, the flow tangency at the wall is specified. As previous numerical implementations failed to give satisfactory results,[5,7,10] a new rotated extrapolation boundary treatment is developed in this paper. The properties at the boundary node are obtained from those of interior points by extrapolating along a unit vector α, which indicates the direction of mininmum variation for a chosen flow property. This vector is set outward normal to the gradient of pressure and is determined for every interior node neighboring the boundary (I_i in Fig. 2). The corresponding pseudopoint (P_i in Fig. 2) is located at the intersection of α and the boundary surface. For the first-order-accurate approach, properties at a pseudopoint represent those of the corresponding interior node. In order to achieve second-order accurate rotated extrapolation, the properties at pseudopoints Q_{P_i} are determined by the following equation:

$$Q_{P_i} = Q_{I_i} + \nabla Q_{I_i} L_{I_i, P_i} \qquad (16)$$

where Q_{P_i} and Q_{I_i} represent the primitive variables at pseudopoint P_i and interior node I_i, respectively, and L_{I_i, P_i} is the position vector from I_i to P_i. After all of the values of Q_{P_i} are obtained, the boundary nodes (B_i in Fig. 2) properties Q_{B_i} can be found from the linear interpolation of Q_{P_i}. Note that the present rotated extrapolation technique is not limited to treating wall boundary conditions, but can also be applied to supersonic outflow boundary. In the present calculations, the pseudopoints are redistributed at every stage of the Runge-Kutta integration.

The numerical experiments indicate that the procedure employed in determining the vector α may result in the following problems: 1) for a flow region possessing a very small pressure gradient, the randomly directed α will lead to the irregular distribution of pseudopoints, and 2) when the vector α is nearly parallel to the boundary surface, it becomes very difficult to accurately locate a pseudopoint. In order to solve these two problems, the pressure gradient at the interior point I_i, $(\nabla p)_{I_i}$ is normalized and filtered by the following weighting formula:

$$(\nabla p)_{I_i}^* = w \frac{(\nabla p)_{I_i}}{(\nabla p)_{I_i}} + (1 - w) t_{I_i} \qquad (17)$$

where

$$w = \text{minimum} \ (1.0, w^*) \qquad (18)$$

$$w^* = \left(\frac{|\nabla p|_{I_i}}{|\nabla p|_{\text{avg}}}\right)\left(\frac{|(\nabla p)_{I_i} \cdot t_{I_i}|}{|\nabla p|_{I_i}}\right) \qquad (19)$$

In Eqs. (17-19), $(\nabla p)_{I_i}^*$ represents the normalized and filtered pressure gradient at interior point I_i. $|\nabla p|_{\text{avg}}$ is the average value of the unfiltered pressure gradients of all interior point
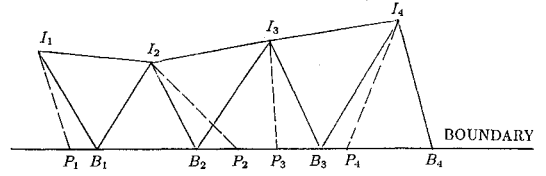

Fig. 2   Configuration of boundary cells for rotated extrapolation.

neighboring the boundary, and t_{I_i} is a unit vector tangent to the boundary surface at interior node I_i. For example, t_{I_4} is parallel to the boundary segment $\overline{B_3 B_4}$ (see Fig. 2). With this filtering process, the value of w approaches zero when the pressure gradient is much smaller than the average value, or when the vector $(\nabla p)_{I_i}$ is almost normal to the unit vector t_{I_i}. Under these limiting conditions, the normalized and filtered pressure gradient $(\nabla p)_{I_i}^*$ is almost equal to the unit vector t_{I_i}, and thus normal extrapolation can be used in both cases. To demonstrate the reliability and accuracy of the rotated boundary condition, supersonic shock reflection at a wall is investigated. The results are compared to the conventional normal extrapolation and characteristic approach, the latter being derived from the characteristic treatment of incompressible flows.[15]

Mesh Generation

All of the computations in this paper were performed on meshes generated by modifying the global/local remeshing algorithms that were proposed by Hwang and Wu.[9] This approach consists of construction of a background grid, specification or computation of remeshing parameters (node spacing, stretching direction, and ratio of stretching), distribution of boundary and interior nodes, triangulation, and combination of triangles into quadrilaterals. The background grid is used to provide a piecewise linear spatial distribution of the remeshing parameters. Nodal points are distributed according to the remeshing parameter, and those nodes are connected into a complete mesh by using the vertex-based triangulation technique. Mixed quadrilateral-triangular meshes are obtained by a combination procedure, which couples two triangles into a new quadrilateral when the common side of the two triangles is the longest one of those two triangles. For the computation of unsteady flow, the remeshing method is localized to minimize the region to be regenerated. This is achieved by recovering those elements and nodes on which the remeshing parameters are not changed significantly. A more detailed description of the mesh generation technique is given in Ref. 9. In the present study, some improvements, including the calculation of node spacing and the concept of dual background grids, are introduced.

Node Spacing

By using the gradient of a key variable φ, the following expression is applied to find the node spacing at the node i:

$$\delta_i^2 \ |\nabla \varphi|_i = \text{const} \qquad (20)$$

where φ is the selected key variable, δ_i the spacing at node i, and $|\nabla \varphi|_i$ the absolute value of the gradient of φ at node i.

In Ref. 9, flow density was selected as the key variable, and the constant was taken as the product of a specified minimum node spacing and the maximum value of the absolute gradients over the domain. However, the use of a maximum absolute gradient may give results that are strongly dependent on the behavior of the single point whose solution gradient is largest. Furthermore, when the flow properties over the entire domain become smooth in some unsteady problems, the number of elements increases significantly since all of the node spacings are almost equal to the specified minimum value. In this work, the constant in Eq. (20) is determined by the product of a specified average node spacing and the average abso-

lute value of the gradients to solve these problems. All node spacings computed by Eq. (20) must be limited to the specified maximum and minimum values.

Dual Background Grids

Both kinds of background grids (primary and secondary) are utilized in this paper to provide a piecewise linear distribution of the remeshing parameters. The primary background grid is essential for the construction of a mesh. This mesh, which consists of only a few elements and nodes, is used to specify the remeshing parameters based on geometrical requirements of the computational domain. The secondary background grid is a complete one on which solutions have been obtained. Remeshing parameters on each node of this background grid are found by the error indicator, a necessary procedure when creating an adaptive mesh. In general, the secondary background grid alone is enough to generate a new mesh. However, when some boundaries of the domain are curved, coarse elements on them are to be avoided, and a certain level of node intensity is needed to maintain a satisfactory shape of the geometry. In this situation, not only is the
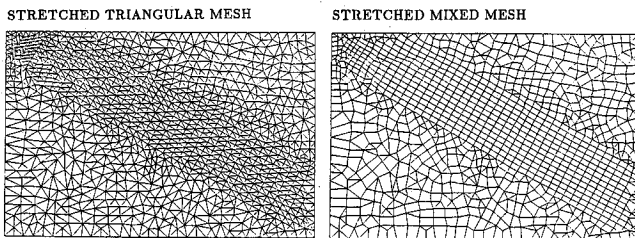

Fig. 3 Meshes for the isolated oblique shock problem: stretched triangles (2046 elements, 1087 nodes) and stretched mixed mesh (1191 elements, 1087 nodes).
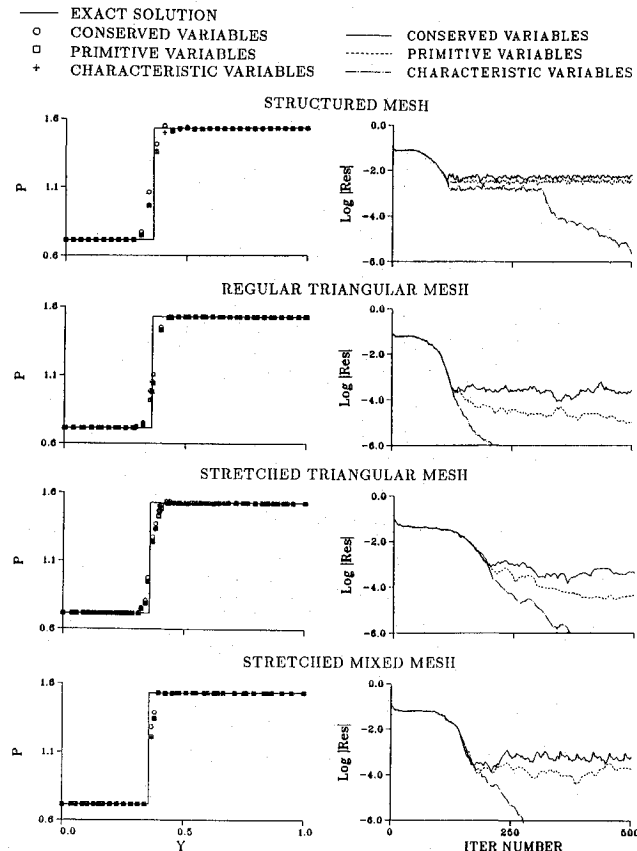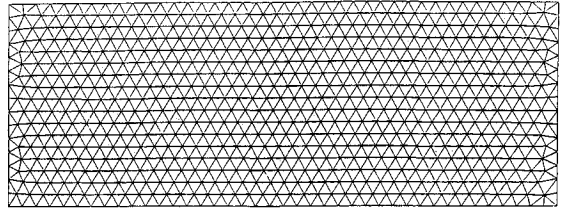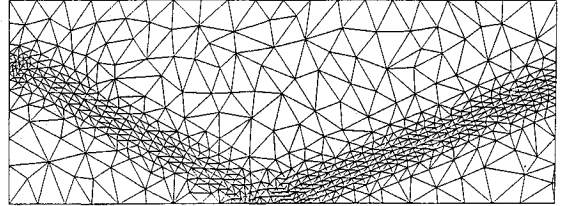

Fig. 4 Pressure distributions along $X = 1.17188$ and the corresponding convergence histories for the isolated oblique shock problem: comparison of interpolation variables on structured quadrilaterals, regular triangles, stretched triangles, and stretched mixed mesh.
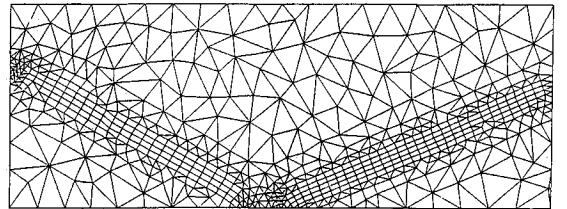

Fig. 5 Meshes for the shock reflection at a wall: regular triangles (1340 elements, 726 nodes), stretched triangles (1159 elements, 621 nodes), and stretched mixed mesh (900 elements, 621 nodes).

secondary background mesh required, but also the primary one. For each node on the secondary background grid, two sets of node spacing are found; one is determined from the error indicator, and the other is obtained by linear interpolation of the node spacings on the primary background mesh. The smaller node spacing is adopted for mesh regeneration. For the computations of transonic flows around single- and two-element airfoils, the technique employing dual background grids is used to generate the adapted mixed meshes.

Results and Discussion

Isolated Oblique Shock

With different interpolation variables in the MUSCL differencing, an isolated oblique shock problem is investigated to show the merit of using characteristic variables in the upwind finite volume approach. In this flow problem, the freestream Mach number and incident shock angle are equal to 2.9 and 29 deg, respectively. On the rectangular 2.0×1.5 computational domain, the following four grid systems are employed: structured quadrilaterals (1024 elements, 1089 nodes), regular triangles (2018 elements, 1071 nodes), stretched triangles (2046 clements, 1087 nodes), and stretched mixed mesh (1191 elements, 1087 nodes). Note that the number and locations of nodes for the stretched mixed mesh are the same as those of the stretched triangular mesh (see Fig. 3).

By using the MINMOD limiter, the conserved, primitive and characteristic interpolation variables are introduced. On the four grid systems, the resulting pressure distributions along $X = 1.17188$ and corresponding convergence histories of maximum density residual are shown in Fig. 4. For the structured quadrilateral mesh, both conserved and primitive variables lead to overshoot in the pressure distributions and limit cycles in convergence histories, whereas the characteristic variables give satisfactory solutions and convergence. These observations are similar to those in Ref. 7. On the unstructured meshes, not one of the three types of interpolation variables cause significant differences in pressure distribution.

However, the characteristic variables still give the best convergence performance where the maximum residual of density can all be reduced to 10^{-6}. In addition to the numerical performance mentioned earlier, the mixed quadrilateral-triangular mesh is capable of resolving an oblique shock with fewer nodes than other grid systems. As we can see from the preceding discussion, the characteristic variables are well suited for the present upwind formation, and they are adopted in the following computations.
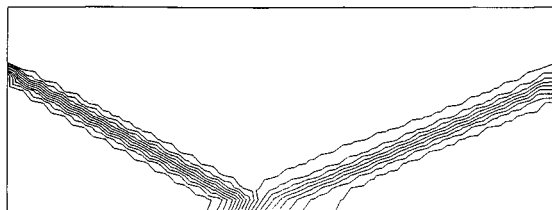
Oblique Shock Reflection at a Wall

To evaluate the accuracy and feasibility of the present boundary treatment, the problem of oblique shock reflection at a wall is studied. In this flow problem, the freestream Mach number and incident shock angle are 2.9 and 29 deg, respectively. On a rectangular 4.0×1.5 computational domain, the following grid systems are employed: the regular triangular, stretched triangular, and mixed quadrilateral-triangular meshes. As shown in Fig. 5, both stretched mesh systems have the same distributions of nodes. Flow properties are specified on the left and upper planes, and the following three types of boundary treatments on the wall surface and outflow plane are used: 1) first-order-accurate normal extrapolation on the wall and exit plane, 2) characteristic extrapolation on the wall and first-order-accurate normal extrapolation on the exit plane, and 3) first-order-accurate rotated extrapolation on both the wall and exit plane. When van Albada et al.'s limiter is introduced on the regular triangular mesh shown on the top of Fig. 5, the resulting Mach number contours (see Fig. 6) indicate that normal extrapolation leads to a significantly smeared oblique shock on the wall surface. Note that, even though the characteristic boundary condition gives better resolution of the shock, small oscillations are generated normal to the wall surface. Similar behavior was also observed in Ref. 10. As evidenced in Fig. 6, the current rotated extrapolation technique provides satisfactory results on both the wall surface and exit plane.

NORMAL EXTRAPOLATION BOUNDARY CONDITION
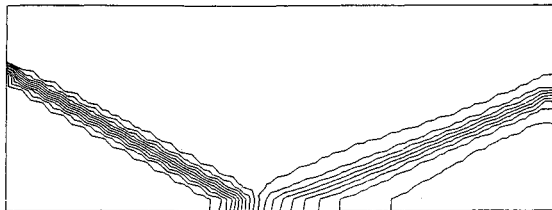
CHARACTERISTIC BOUNDARY CONDITION

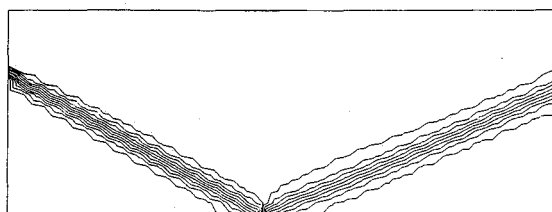ROTATED BOUNDARY CONDITION

Fig. 6 Mach number contours (level = 0.05) of the shock reflection at a wall: comparison of boundary conditions on the regular triangular mesh shown in Fig. 5.
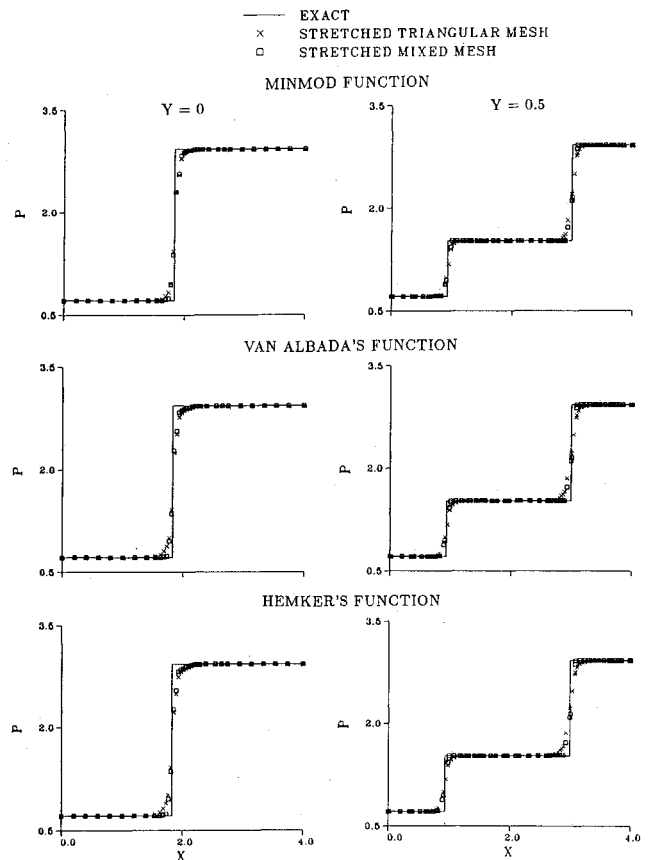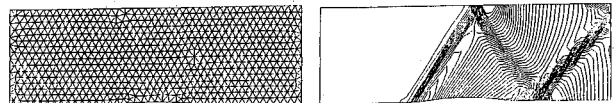

Fig. 7 Pressure distributions along $Y = 0$ and 0.5 for the shock reflection at a wall.
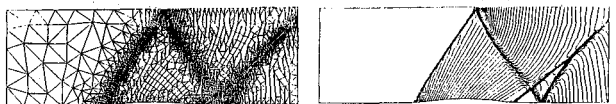

Fig. 8 Initial triangular mesh, first and final adapted mixed meshes, and the corresponding pressure contours for supersonic flow passing through a channel with a 4% circular arc bump.

By using rotated boundary conditions and three types of limiters on the stretched triangular and mixed quadrilateral-triangular meshes, the resulting pressure distributions along $Y = 0$ and 0.5 are presented in Fig. 7. From the results illustrated in Figs. 5 and 7, the use of mixed meshes has the following advantages: 1) fewer elements are required, 2) shocks are resolved with a minimum number of transition nodes, and 3) the results are less sensitive to the limiters. From this discussion, it is apparent that rotated boundary conditions and mixed quadrilateral-triangular meshes should be used in the following computations.

Supersonic Flow Passing Through a Channel with a 4% Circular Arc Bump

For the case of supersonic flow ($M_\infty = 1.4$) passing through a channel with a 4% circular arc bump, the present upwind
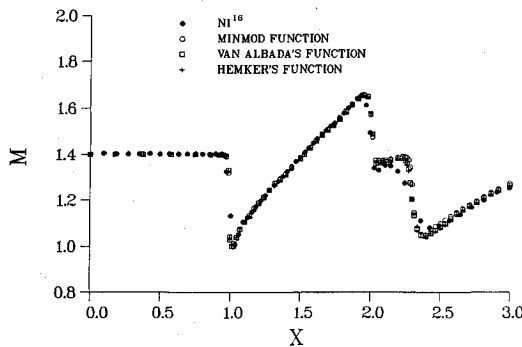
Fig. 9   Mach number distributions along the lower wall for supersonic flow passing through a channel with a 4% circular arc bump.

INITIAL TRIANGULAR MESH: 6927 ELEMENTS, 3561 NODES

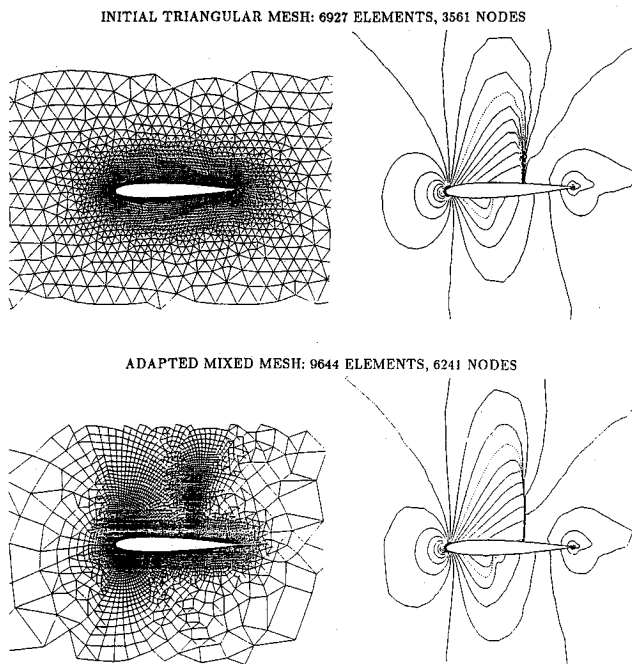ADAPTED MIXED MESH: 9644 ELEMENTS, 6241 NODES

Fig. 10   Transonic flow over the NACA-0012 airfoil: the initial grid, adapted mixed mesh, and the corresponding Mach number contours.

approach, utilizing second-order-accurate rotated boundary treatment and characteristic interpolation variables, is implemented on mixed quadrilateral-triangular meshes. When the MINMOD limiter is applied, the initial triangular mesh, first and final (third) adapted mixed meshes, and the corresponding pressure contours clearly indicate the shock structures in the flowfield (see Fig. 8). The proposed rotated boundary treatment gives satisfactory results on the wall surface and exit plane. For the other two limiters, similar results are obtained. On the final adapted mesh (see Fig. 8), the Mach number distributions along the lower wall surface are plotted in Fig. 9. The numerical solutions are not sensitive to the limiters, and the shocks are well resolved in comparison to Ni's results.[16]

Transonic Flow over the NACA-0012 Airfoil

To prove the capability of the present upwind approach for solving transonic external flows, a NACA-0012 airfoil flow with a Mach number of 0.8 and the angle of attack equal to 1.25 deg is investigated. In this study, the outer boundary is taken as a rectangle of 21 × 20 chords. The second-order-accurate rotated boundary condition is used on the airfoil surface, and one-dimensional characteristic analysis is applied to the far-field boundary. In order to keep the mesh sizes uniform near the airfoil, pure triangles are used in this region. Van Albada et al.'s limiter is used to obtain the solutions on

the initial triangular and adapted mixed quadrilateral-triangular meshes. The grids are shown together with their corresponding Mach number contours in Fig. 10. From an examination at these results on the adapted mixed meshes, it is apparent that high-resolution results are achieved. For the three kinds of limiters, the pressure coefficient distributions
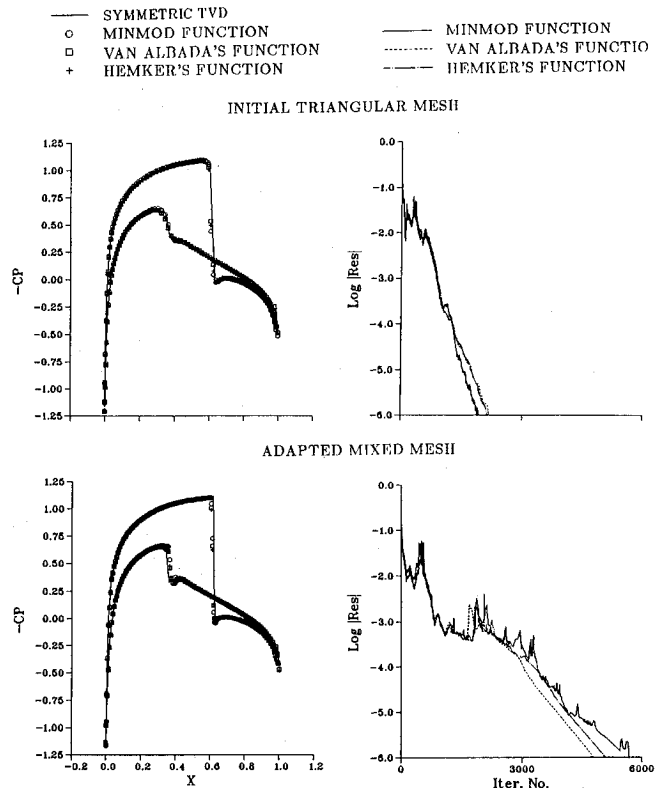

Fig. 11   Pressure coefficient distributions along the airfoil surface and the corresponding convergence histories for the transonic flow over the NACA-0012 airfoil.
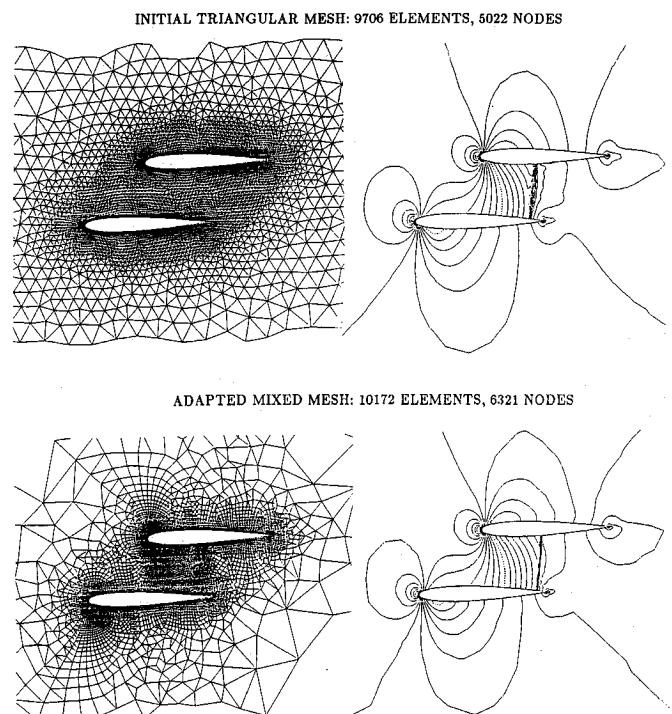
INITIAL TRIANGULAR MESH: 9706 ELEMENTS, 5022 NODES

ADAPTED MIXED MESH: 10172 ELEMENTS, 6321 NODES

Fig. 12   Transonic flow around a two-element airfoil: the initial grid, adapted mixed mesh, and the corresponding Mach number contours.
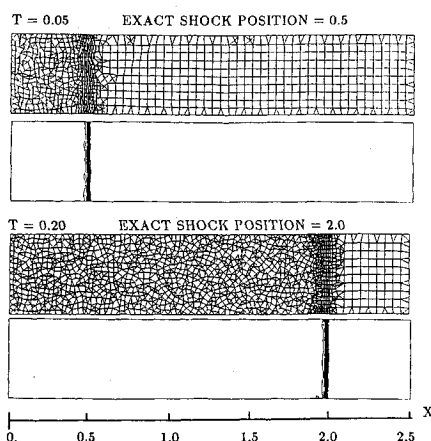
Fig. 13 Shock propagation in a channel: adapted mixed meshes and the corresponding pressure contours at $T = 0.05$ and 0.2.

along the airfoil surface and the convergence histories are plotted in Fig. 11. The shock positions and the strengths are comparable to those obtained by the locally implicit symmetrical total-variation-diminishing scheme,[2] whose adapted mesh is composed of pure triangles. In a similar manner to previous test examples, different limiters do not introduce significantly different results when the current approach is applied on the mixed quadrilateral-triangular mesh.

Transonic Flow Around a Two-Element Airfoil

To demonstrate the availability of the present approach for computing flow passing through a domain with complex geometry, the flow around a two-element airfoil is investigated. The transonic flow considered here is of a staggered biplane configuration consisting of two NACA-0012 airfoils with a freestream Mach number of 0.7 and an angle of attack equal to zero. In this example, the outer boundary is taken as being a rectangle of 21×20 chords and the boundary treatments remain the same as those for the single airfoil flow. Hemker and Koren's limiter is used to obtain the solutions on the initial triangular and adapted mixed quadrilateral-triangular meshes. The grids are shown together with their corresponding Mach number contours in Fig. 12. An inspection of the grid distributions and the Mach number contours indicates that the shock between two airfoils is better resolved on the mixed mesh system.

Shock Propagation in a Channel

To evidence the ability of the present adaptive finite volume approach to handle the unsteady flows, a shock propagation problem is studied. In this example, a strong shock with a shock Mach number of 10.0 moves to the right along a 2.5 $\times 0.5$ rectangular channel from position $X = 0.0$ at $T = 0.0$. By using the local remeshing technique,[9] the mesh is regenerated every 20 time steps. Linear interpolation is used to transfer the variables onto a newly generated mesh. As mentioned in Ref. 9, this nonconservative interpolation procedure does not introduce significant error in the numerical results. Solutions are achieved by advancing at a constant time step corresponding to a Courant number of 0.1, which is based on minimum node spacing. By applying van Albada et al.'s limiter, the adapted mixed meshes and the corresponding pressure contours at $T = 0.05$ and 0.2 are obtained and plotted in Fig. 13. In comparison to the exact shock positions, the shock is propagating with satisfactorily high resolution and time accuracy. From the preceding discussion, it is obvious that the present adaptive finite volume upwind approach, which is coupled with the local remeshing technique, provides an effective and accurate way for investigating unsteady flow problems.

Conclusions

In the present paper, a solution-adaptive cell-vertex finite volume upwind approach has been developed to solve the

unsteady Euler equations on unstructured mixed quadrilateral-triangular meshes, where the quadrilaterals are directionally stretched in the flow regions having one-dimensional features. This approach incorporates Runge-Kutta time integration, Roe's Riemann solver, MUSCL differencing with characteristic interpolation variables, a new treatment of the rotated extrapolation boundary condition, and an improved technique of solution-adaptive mesh regeneration. In the computations of an isolated oblique shock, the characteristic interpolation variables give better results than conserved and primitive variables. For an oblique shock reflection at a wall, the present rotated extrapolation boundary treatment provides satisfactory results on the wall surface and exit plane in comparison with the normal extrapolation and characteristic boundary condition. From the two examples just mentioned, the advantages of using mixed quadrilateral-triangular meshes are presented and confirmed. To demonstrate the reliability, accuracy, and robustness of the current approach, supersonic flow passing through a channel with a 4% circular arc bump, transonic flows around single- and two-element airfoils, as well as unsteady shock propagation in a channel are investigated. The numerical experiments indicate that the present solution procedure provides accurate and high-resolution results with good performance of convergence for compresssible, inviscid, steady, and unsteady flows.

References

[1]Mavriplis, D. J., "Accurate Multigrid Solution of the Euler Equations on Unstructured and Adaptive Meshes," *AIAA Journal*, Vol. 28, No. 2, 1990, pp. 213–221.

[2]Hwang, C. J., and Liu, J. L., "Locally Implicit Total-Variation-Diminishing Schemes on Unstructured Triangular Meshes," *AIAA Journal*, Vol. 29, No. 10, 1991, pp. 1619–1626.

[3]Barth, T. J., and Jespersen, D. C., "The Design and Application of Upwind Schemes on Unstructured Meshes," AIAA Paper 89-0366, Jan. 1989.

[4]Barth, T. J., and Frederickson, P. O., "Higher Order Solution of the Euler Equations on Unstructured Grids Using Quadratic Reconstruction," AIAA Paper 90-0013, Jan. 1990.

[5]Whitaker, D. L., Grossman, B., and Lohner, R., "Two-Dimensional Euler Computations on a Triangular Mesh Using an Upwind, Finite-Volume Scheme," AIAA Paper 89-0470, Jan. 1989.

[6]Roe, P. L., "Approximate Riemann Solvers, Parameter Vectors, and Difference Schemes," *Journal of Computational Physics*, Vol. 43, No. 2, Oct. 1981, pp. 357–372.

[7]Dadone, A., and Grossman, B., "A Rotated Upwind Scheme for the Euler Equations," AIAA Paper 91-0635, Jan. 1991.

[8]Kontinos, D. A., and McRae, D. S., "An Explicit, Rotated Upwind Algorithm for Solution of the Euler/Navier-Stokes Equations," *Proceedings of the AIAA 10th Computational Fluid Dynamics Conference* (Honolulu, HI), June 1991, pp. 47–59 (AIAA Paper 91-1531).

[9]Hwang, C. J., and Wu, S. J., "Global and Local Remeshing Algorithms for Compressible Flows," *Journal of Computational Physics*, Vol. 102, No. 1, Sept. 1992, pp. 98–113.

[10]Dadone, A., "A Physical-Numerical Treatment of Impermeable Boundaries in Compressible Flow Problems," *Proceedings of the Fourth International Symposium on Computational Fluid Dynamics*, Vol. 1, Univ. of California, Davis, CA, Sept. 1991, pp. 258–263.

[11]Shu, C. W., "Total-Variation-Diminishing Time Discretizations," *SIAM Journal on Scientific and Statistical Computing*, Vol. 9, No. 6, 1988, pp. 1073–1084.

[12]Anderson, W. K., Thomas, J. L., and van Leer, B., "A Comparison of Finite Volume Flux Vector Splittings for the Euler Equations," AIAA Paper 85-0122, Jan. 1985.

[13]van Albada, G. D., van Leer, B., and Roberts, W. W., Jr., "A Comparative Study of Computational Methods in Cosmic Gas Dynamics," *Astronomy and Astrophysics*, Vol. 108, No. 1, 1982, pp. 76–84.

[14]Hemker, P. W., and Koren, B., "Multigrid, Defect Correction and Upwind Schemes for the Steady Navier-Stokes Equations," Synopsis, HERMES Hypersonic Research Program Meeting, Stuttgart, Nov. 1987.

[15]Pan, D., and Chakravarthy, S. R., "Unified Formulation for Incompressible Flows," AIAA Paper 89-0122, Jan. 1989.

[16]Ni, R. H., "A Multiple-Grid Scheme for Solving the Euler Equations," *AIAA Journal*, Vol. 20, No. 11, 1982, pp. 1565–1571.